JOM, Vol. 73, No. 8, 2021
https://doi.org/10.1007/s11837-021-04738-3

TECHNICAL ARTICLE

Effect of Al Addition on Microstructure and Tensile Properties of Mg-8Li-3Al Alloy

ZILONG ZHAO,[1] BAOYU DUAN,[2] JIE YING,[1,4] and LIANG LI[3]

1.—School of Chemical Engineering and Technology, Sun Yat-sen University, Zhuhai 519082, China. 2.—School of Materials Science and Engineering, Inner Mongolia University of Science and Technology, Baotou 014010, China. 3.—School of Physics, Engineering and Computer Science, University of Hertfordshire, Hatfield AL109AB, UK. 4.—e-mail: whutyingjie@gmail.com

The microstructure and mechanical properties of Mg-8Li and Mg-8Li-3Al (wt.%) alloys have been investigated. Addition of Al to Mg-8Li alloy results in precipitation of Al-Li phase in the as-rolled Mg-8Li-3Al alloy. The ultimate tensile strength and yield strength of Mg-8Li-3Al alloy reach 238 MPa and 198 MPa, as compared with 147 MPa and 126 MPa for Mg-8Li alloy, representing increases of $\sim 62\%$ and $\sim 57\%$, respectively. These enhanced mechanical properties can be ascribed to precipitation strengthening by Al-Li phase and the orientation of α-Mg phase and β-Li phase. The grains in Mg-8Li-3Al alloy obtained via deformation processing are mainly composed of substructured grains, so the strength of the alloy is improved while maintaining high plasticity.

INTRODUCTION

Magnesium (Mg) alloys have received extensive attention because of their beneficial features of high specific strength, high specific stiffness, and good castability, making them promising for applications in many fields such as transportation and aerospace.[1–3] It is noted that the majority of Mg alloys products have been fabricated via casting so far. However, further enhancement of their mechanical properties (strength, ductility, toughness, etc.) is essential to extend their specific applications in transport tool components, personal electronic devices, and biodegradable medical implants.[4–12] In recent years, deformation processing has been demonstrated to be a highly effective method to enhance the above-mentioned mechanical properties of Mg alloys.[13] Thus, wrought Mg alloys, especially Mg-Li alloys, are attracting increasing attention due to their outstanding lightweight nature and excellent deformation properties.[14–18]

Mg normally shows relatively poor deformability at room temperature due to its intrinsic hexagonal close-packed (HCP) structure along with limited slip systems.[19,20] An efficient method to improve the deformability and ductility of Mg is to form Mg-Li alloy by adding body-center cubic (BCC)-structured Li.[21,22] When the Li content is less than 5.5 wt.%, Mg-Li alloy retains the HCP crystal structure of Mg due to the formation of solid solution of Li in α-Mg.[23] The microstructure of Mg-Li alloy transforms from a single-phase to a double-phase structure including HCP-structured α-Mg and BCC-structured β-Li when the Li content lies between 5.5 wt.% and 11 wt.%, and further to single-phase BCC-structured β-Li when the Li content exceeds 11 wt.%.[24] Because of the more active slip systems and lower strength of BCC-structured β-Li in comparison with HCP-structured α-Mg, Mg-Li alloy with double-phase structure commonly shows improved deformability and ductility but decreased strength.[22] Therefore, for Mg-Li alloy, it is also necessary to enhance its strength for practical applications.

Addition of other elements have been proved to be an effective method for enhancing the strength of Mg-Li alloy. For instance, addition of Al-Si eutectic alloy to Mg-8Li alloy can improve its strength by formation of Mg_2Si phase.[25] Al addition can result in significant age hardening of Mg-Li alloy by formation of AlLi and $Mg_{17}Al_{12}$ precipitates.[26] All the cited works indicate the great influence of Al

(Received February 22, 2021; accepted May 20, 2021; published online June 7, 2021)

addition on the properties of Mg-Li alloy and have enhanced our understanding of Mg-Li alloy. Moreover, many scholars have reported that alloying and deformation strengthening can comprehensively improve the mechanical properties of alloys.[27,28] However, few studies have elucidated the deformation behavior and microstructural change of Mg-Li alloy on addition of Al, where characterization of the grain orientation is required to correlate the microstructural change, e.g., grain orientation, with the deformation mechanism.

The aim of this study is to investigate the effect of Al addition on the microstructural change and deformation behavior of Mg-8Li alloy. To achieve this, the microstructures were examined by scanning electron microscopy (SEM) and transmission electron microscopy (TEM). Tensile tests were carried out to determine the mechanical properties of Mg-8Li and Mg-8Li-3Al alloys. The microstructures and mechanical properties of Mg-8Li and Mg-8Li-3Al alloys were compared and are discussed.

EXPERIMENTAL PROCEDURES

The magnetic-leviation, high-frequency induction melting technique was used to prepare Mg-8Li and Mg-8Li-3Al alloys (all in wt.% unless otherwise stated). Pure magnesium, pure lithium, and/or aluminum were melted under Ar atmosphere initially, then cast into a water-cooled copper mold (Φ30 mm × 60 mm). The ingot was cut into round plates with size of Φ30 mm × 10 mm, then annealed at 300°C for 60 min. The heat-treated sample was rolled into a 1.6-mm-thick sheet after eight rolling passes with a ~ 20% thickness decrease in each pass. The rolls (Φ130 mm) were preheated to 150°C and maintained at this temperature during the rolling process using an internal resistance wire heating coil. Subsequently, all the rolled specimens were annealed at 150°C for 60 min.

The microstructures were examined by SEM (JSM-7800F, JEOL, Japan) equipped with an Oxford electron backscattered diffraction system, and TEM (JEOL-2100F, JEOL, Japan). The texture of the grains was characterized by electron backscatter diffraction (EBSD) measurement with a step size of 3 μm. The samples for SEM and EBSD characterization were prepared by using an ion milling apparatus (CP, IB-19530, JEOL). The ion-polished sample had an area of 8 mm × 4 mm in the rolling direction. For TEM observation, the sample was ion-milled in a Leica EM RES102 machine.

Tensile tests were conducted to evaluate the mechanical properties of the materials. For tensile tests, specimens having a gauge length of 15 mm, width of 3 mm, and thickness of 1.5 mm were machined from the rolled plates. The tensile tests were performed on an electronic universal testing machine (CMT5205, MTS Systems Corporation, US) based on the ASTM E8/E8M-2011 standard. The displacement rate was 0.5 mm/min. In total, five tensile tests for each sample condition were repeated to obtain good statistics of the results.

RESULTS AND DISCUSSION

The typical engineering stress–strain curves for Mg-8Li and Mg-8Li-3Al alloys are displayed in Fig. 1. Table I summarizes the mechanical properties of Mg-8Li and Mg-8Li-3Al alloys. The ultimate tensile strength (UTS) of Mg-8Li and Mg-8Li-3Al alloys was found to be 147 MPa and 238 MPa, respectively. Each experiment was performed under different conditions of factor proportions.[29] The yield strength (YS) of the Mg-8Li and Mg-8Li-3Al alloys was determined to be 126 MPa and 198 MPa, respectively. The data show that the tensile strength of the two-phase Mg-8Li alloy is significantly improved by the addition of 3% Al, while the elongation remained at a relatively high level. The results presented in Table I indicate that addition of 3% Al improved the comprehensive mechanical properties of Mg-8Li-3Al alloy. The fracture elongation (FE) of Mg-8Li-3Al alloy (25.5%) showed a little decline in comparison with that of Mg-8Li alloy (38.0%). The UTS and YS were improved by ~ 62% and ~ 57%, respectively, as compared with those of Mg-8Li alloy.

To reveal the reason for the enhanced tensile properties of Mg-8Li-3Al alloy, its microstructural change and deformation behavior were investigated. Figure 2 shows SEM images of as-rolled and annealed Mg-8Li and Mg-8Li-3Al alloys. It is clearly seen that both alloys possessed a dual-phase

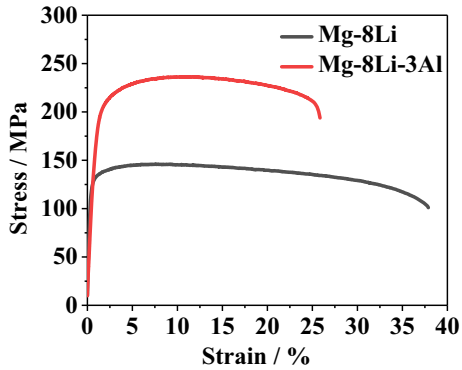

Fig. 1. Typical engineering stress–strain curves of as-rolled and annealed Mg-8Li and Mg-8Li-3Al alloys.

Table I. Mechanical properties of as-rolled and annealed Mg-8Li and Mg-8Li-3Al alloys

Alloy	UTS (MPa)	YS (MPa)	FE (%)
Mg-8Li	147	126	38.0
Mg-8Li-3Al	238	198	25.5

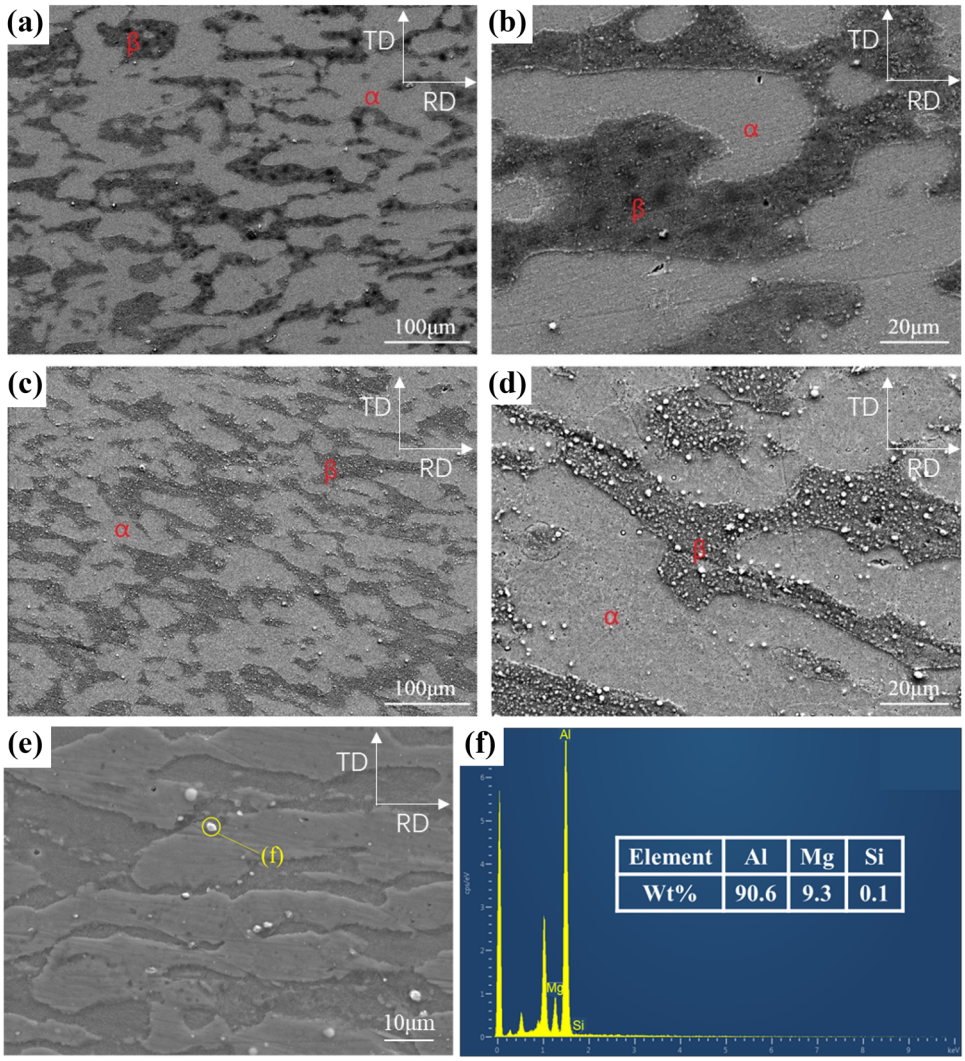

Fig. 2. SEM images of as-rolled and annealed (a, b) Mg-8Li and (c, d) Mg-8Li-3Al alloys. (e) Enlarged SEM image of Mg-8Li-3Al alloy and (f) corresponding EDS point elemental contents of a white precipitate indicated in (e). White arrows in SEM images indicate the rolling direction.

microstructure, in which the black–gray structure is β-phase[30] while the gray–white one is α-phase. Comparing Fig. 2a with Fig. 2c, it can be seen that there are a lot of white precipitates in Mg-8Li-3Al alloy, but no precipitates in Mg-8Li alloy. The white precipitates are Al-Li phase according to a previous report.[31] To further observe the structure of the alloy, Fig. 2b and d shows enlargements. It is obvious that there are no precipitates in Mg-8Li alloy, but precipitates in Mg-8Li-3Al alloy. As shown in Fig. 2e and f, energy-dispersive spectrometry (EDS) elemental analysis revealed that the white precipitate in the β-phase is Al-Li phase with high Al content of 90.6 wt.%. At the same time, one can see that there are more precipitates in the β-phase structure. The precipitation strengthening mechanism of Al in single α-phase alloy and single β-phase alloy has been reported by Liang et al.[2] and Xu et al.,[32] respectively. It is concluded that the solid-solution strengthening effect of Al and the second-phase strengthening of Al-Li compounds are responsible for the precipitation strengthening of Al.

To further analyze the morphology of phases and examine the detailed structure within the phases in Mg-8Li-3Al alloy, the sample was observed by TEM. Figure 3 shows TEM images of white granular precipitates region in Fig. 2d. The light-grey particle in Fig. 3a contains two black cores with size of 100 nm to 200 nm. For each small black core, there is a circular arc line surrounding it, suggesting a typical Frank–Read (F–R) dislocation increment mechanism.[33] Figure 3b shows the selected-area diffraction (SAED) pattern of the precipitate particle, revealing [01$\bar{1}$1] band axis diffraction of HCP structure. These results suggest that the particle and the two cores were pinned by the formation of the dislocation loops around them, thus causing a stress zone due to the pinning effect. According to dispersion strengthening theory and dislocation theory,[34,35] when the size of the precipitate phase

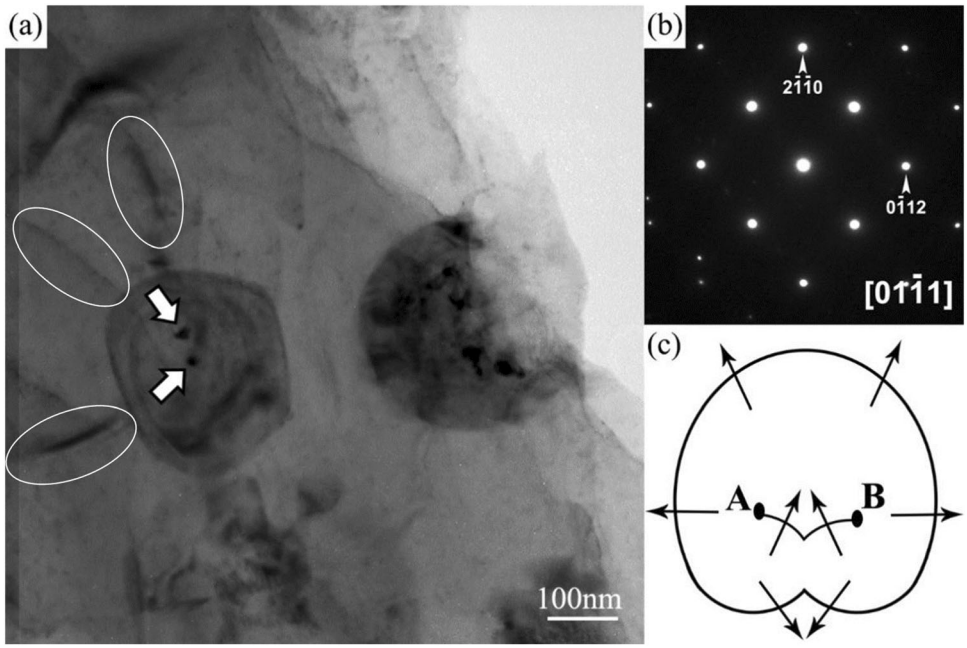

Fig. 3. TEM image (a) and SAED pattern (b) of as-rolled and annealed Mg-8Li-3Al alloy. The white ovals show the dislocations in (a). (c) Schematic illustration of dislocation increment mechanism of Mg-8Li-3Al alloy.

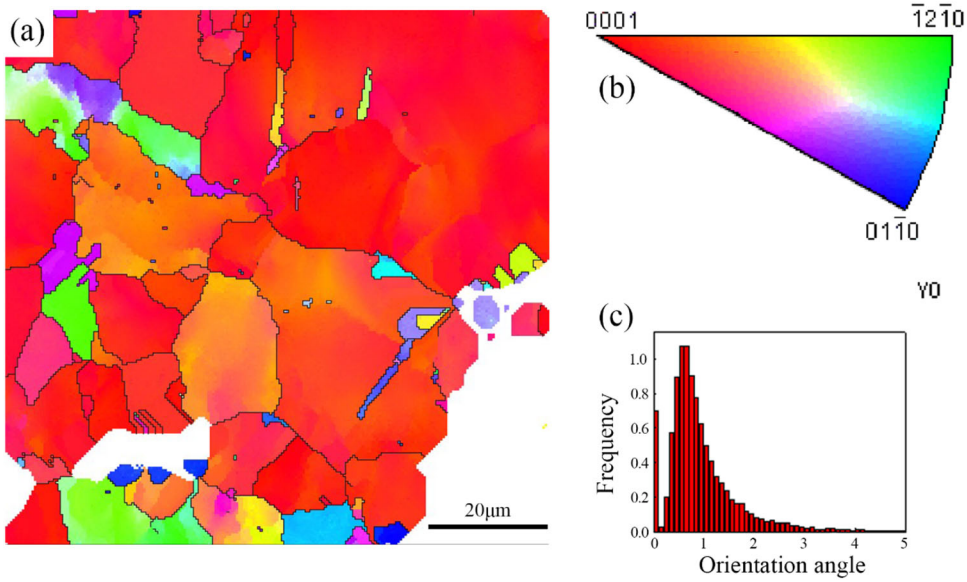

Fig. 4. Grain orientation mapping (a) and quantification of grain frequency as a function of orientation angle (b) of as-rolled and annealed Mg-8Li-3Al alloy. (c) Orientation angle distribution.

decreases to the nanoscale, the precipitates can not only improve the strength of the alloy but also maintain its good plasticity. Figure 3c shows a schematic of the Frank–Read (F–R) dislocation increment mechanism, revealing several edge dislocations formed in the deformation processing, which are blocked in the process of motion and precipitation, playing a strengthening effect on Mg-8Li-3Al alloy.[34]

The microstructure and grain orientation of as-rolled and annealed Mg-8Li-3Al alloy are shown in Fig. 4. The red regions represent α-phase grains, and the twin structures are clearly identified in those regions. According to previous study,[33] α-phase has HCP lattice structure and exhibits relatively poor plastic deformability. Twining structures are frequently observed within the α-phase grains.[24] As seen in Fig. 4a, the orientation of α-phase is close to the [0001] direction, indicating that the basal

texture is relatively strong. The β-phase is mostly green and yellow, indicating that the β-phase orientation experienced a large deflection in the matrix, being predominantly inclined to $[\bar{1}2\bar{1}0]$ orientation. In addition, it can be observed from the inside of the red regions that the sizes of the α-phase grains present a bimodal characteristic with different orientations (Fig. 4b). This is due to the strength discrepancy between the α- and β-phase and their different rotation during rolling processing.[24] It can be seen from Fig. 4c that the grains are mainly small-angle grains, indicating significant strengthening and toughening of Mg-8Li-3Al alloy.[35]

Figure 5 shows the recovery, recrystallization, and grain size distribution of as-rolled and annealed Mg-8Li-3Al alloys, in which the blue regions are recrystallized, the red regions are deformed, and the yellow regions are the substructure having coherent interface. It can be seen in Fig. 5a that the substructure regions account for the largest area, the recrystallized regions are localized, and the deformed regions are mainly distributed around the grain boundary. This indicates that recrystallization had just occurred, and the grains were mainly in the substructure state. The red deformed grains are mainly distributed along the large-grain boundaries. As β-phase is easily oxidized and not easily characterized by EBSD, only the HCP α-phase is presented in this figure. Due to the limited slip system, the deformation of magnesium alloy with HCP structure can be adjusted by a twinning mechanism during rolling at room temperature.[34]

The β-phase with BCC lattice structure has relatively low strength but good plasticity.[34] Therefore, the β-phase and $\alpha + \beta$ phase interface regions provide the major plastic deformation during rolling, and the α-phase provides less plastic deformation. Recrystallization occurs when the severe deformation reaches the critical recrystallization strain. The recrystallized grains are equiaxed and relatively small, which improves the plastic deformation capacity of the material. No twins are observed in the large deformation region of BCC phase, because there are more slip systems of BCC structure than hcp phase, and plastic deformation is more likely to be initiated by more slip systems.[35] As a result, twinning is suppressed and no twins are observed in the β-phase. The blue region is formed due to the recrystallization process. Due to the large number of dislocations accumulated in the large deformation process, the deformation energy increases. In the subsequent heat treatment, both static recovery and static recrystallization took place simultaneously. Meanwhile, recrystallization occurs in the more deformable local regions that are composed of α- and β-phase, while most of the other regions are static recovery. As shown in Fig. 5b, the ratios of recrystallized, substructured, and deformed grains are 9%, 66%, and 25%, respectively. The 66% substructured grains and 25% deformed grains could respectively ensure the good strength and improved plasticity of Mg-8Li-3Al alloy.[25] The grain size distribution of Mg-8Li-3Al alloy is shown in Fig. 5c, indicating quite a high ratio of grain diameters less than 10 μm, in

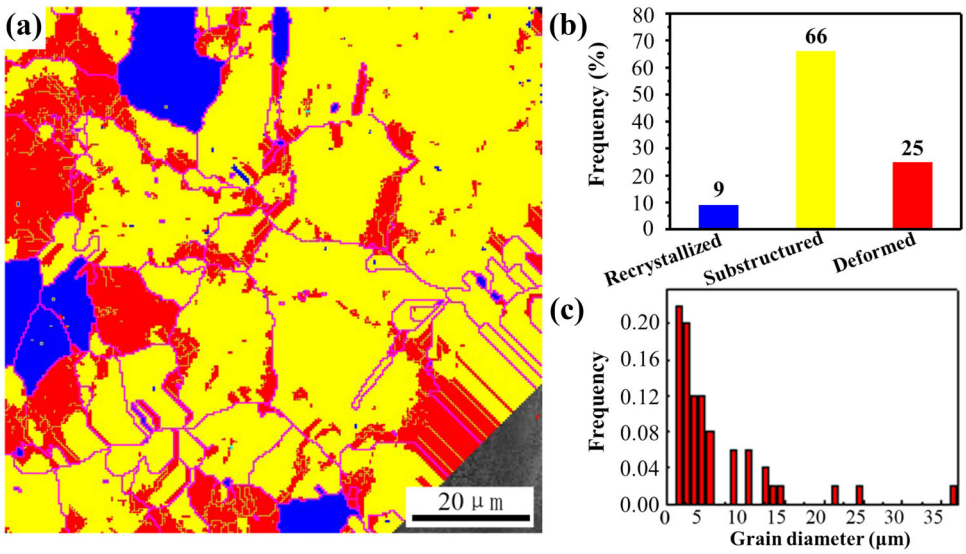

Fig. 5. EBSD analysis of as-rolled and annealed Mg-8Li-3Al alloy: (a) different types of grains in the alloy; blue, yellow, and red color represent recrystallized, substructured, and deformed grains, respectively; (b) frequency of recrystallized, substructured, and deformed grains; (c) grain size distribution (Color figure online).

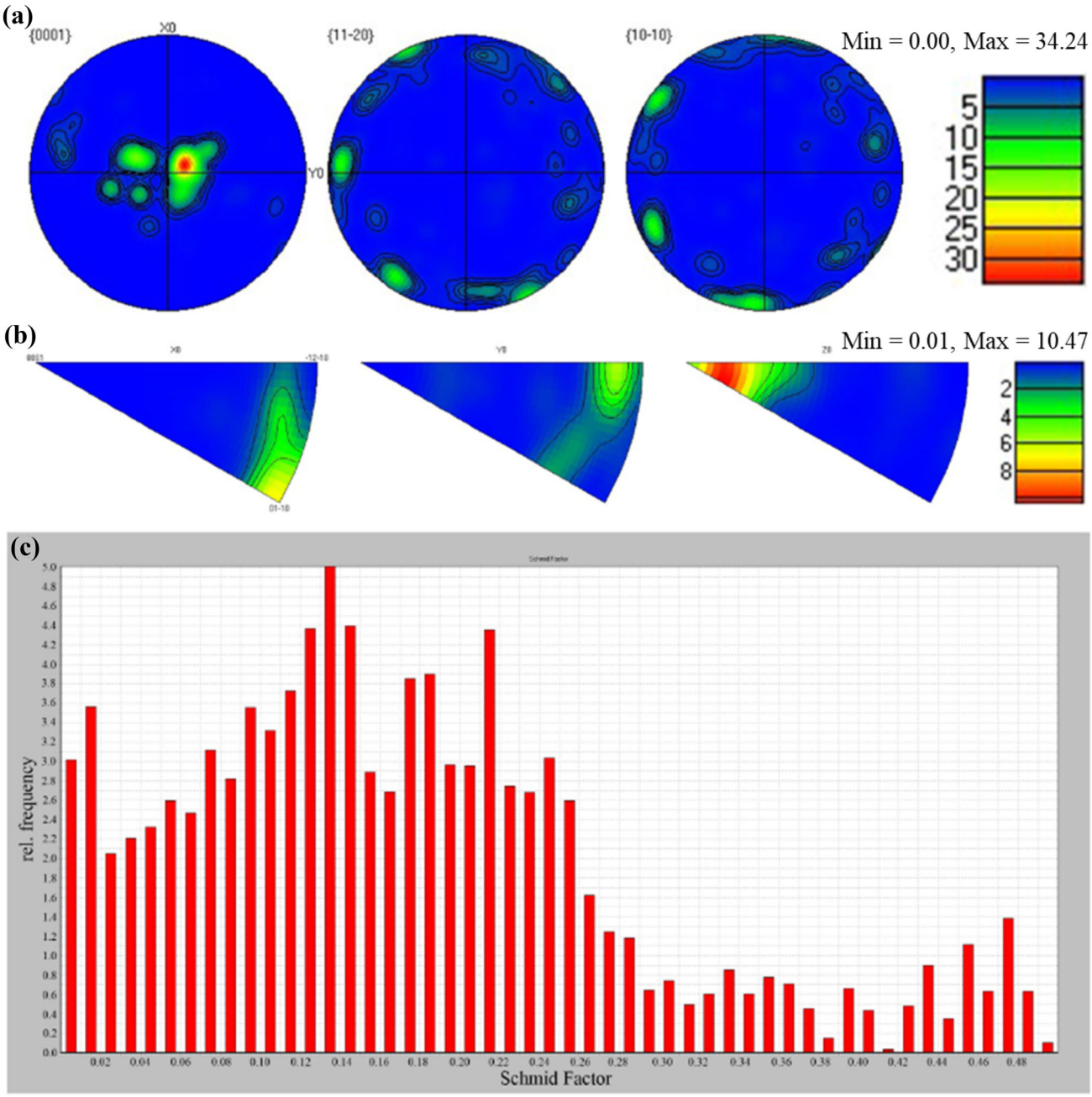

Fig. 6. EBSD analysis of as-rolled and annealed Mg-8Li-3Al alloy: (a) pole figure, (b) inverse pole figure, and (c) Schmid factor.

accordance with the finding of the small size of recrystallized and deformed grains from Fig. 5a, where the small size of deformed grains is attributed to deformation and the small size of recrystallized grains is ascribed to the fast deformation rate, resulting in the lack of growth of these grains.[36]

Figure 6 shows the pole figure, inverse pole figure, and Schmid factor for as-rolled and annealed Mg-8Li-3Al alloy. It can be seen from this figure that a strong basal texture (0001) is formed in the alloy after rolling, indicating that more basal slips occurred during deformation. It is difficult for other slips to initiate because their critical shear stresses are much larger than those of basal slips.[22] In the pole figure, the maximum pole intensity is 34.24, and the minimum is 0.00. Meanwhile, in the reverse pole figure, the maximum pole intensity is 10.47 and the minimum is 0.01. This reveals that sliding on the basal plane for β-phase of Mg-8Li-3Al alloy is responsible for the deformation mechanism during

the rolling process, while for the α-phase sliding on the basal plane and twinning coexist and are responsible for the deformation behavior.

CONCLUSION

Mg-8Li and Mg- 8Li-3Al alloys were fabricated via deformation processing and their microstructure and mechanical properties fully investigated. It is proved that addition of 3% Al to Mg-8Li greatly enhanced its tensile mechanical properties, with an improvement of $\sim$ 62% and $\sim$ 57% in the UTS and YS, respectively. This improvement can be attributed to precipitation strengthening by Al-Li phase and the orientation of α-Mg phase and β-Li phase. The grain size and orientation of the α-Mg phase are not uniform because the different mechanical properties of the α-Mg phase and β-Li phase lead to uneven force during the rolling. In the case of Mg-8Li-3Al alloy, the grains obtained by the deformation mainly consist of substructured grains, so that the strength of the alloy is improved while maintaining high plasticity.

CONFLICT OF INTEREST

The authors declare that they have no conflicts of interest.

ACKNOWLEDGEMENTS

This work was supported by the Fundamental Research Funds for the Central Universities (20lgpy77), Guangdong Basic and Applied Basic Research Foundation (No. 2019A1515110436), and Natural Science Foundation of Inner Mongolia, China (No. 2018MS05038).

REFERENCES

1. B. Guan, Y. Xin, X. Huang, P. Wu, and Q. Liu, *Acta Mater.* 173, 142. (2019).
2. Z.L. Zhao, Z.W. Sun, W. Liang, Y.D. Wang, and L.P. Bian, *Mater. Sci. Eng. A.* 702, 206. (2017).
3. B. Smola, I. Stulıková, F. Von Buch, and B.L. Mordike, *Mater. Sci. Eng. A* 324, 113. (2002).
4. A. Atrens, M. Liu, and N.I.Z. Abidin, *Mater. Sci. Eng. B* 176, 1609. (2011).
5. N.I.Z. Abidin, B. Rolfe, H. Owen, J. Malisano, D. Martin, J. Hofstetter, P.J. Uggowitzer, and A. Atrens, *Corros. Sci.* 75, 354. (2013).
6. C. Taltavull, Z. Shi, B. Torres, J. Rams, and A. Atrens, *J. Mater. Sci.: Mater. Med.* 25, 329. (2014).
7. R. Willumeit, J. Fischer, F. Feyerabend, N. Hort, U. Bismayer, S. Heidrich, and B. Mihailova, *Acta Biomater.* 7, 2704. (2011).
8. H. Hornberger, S. Virtanen, and A.R. Boccaccini, *Acta Biomater.* 8, 2442. (2012).
9. Y. Ding, C. Wen, P. Hodgson, and Y. Li, *J. Mater. Chem.* 2, 1912. (2014).
10. F. Witte, *Acta Biomater.* 6, 1680. (2010).
11. N. Hort, Y. Huang, D. Fechner, M. Störmer, C. Blawert, F. Witte, H. Drücker, R. Willumeit, K.U. Kainer, and F. Feyerabend, *Acta Biomater.* 6, 1714. (2010).
12. J. Qiao, H. Jia, and P.K. Liaw, *Mater. Sci. Eng. R* 100, 1. (2016).
13. N.V. Dudamell, I. Ulacia, F. Gálvez, S. Yi, J. Bohlen, D. Letzig, I. Hurtado, and M.T. Pérez-Prado, *Mater. Sci. Eng. A.* 532, 528. (2012).
14. J. Kuhlmann, I. Bartsch, E. Willbold, S. Schuchardt, O. Holz, N. Hort, D. Höche, W.R. Heineman, and F. Witte, *Acta Biomater.* 9, 8714. (2013).
15. B.L. Mordike, and T. Ebert, *Mater. Sci. Eng. A* 302, 37. (2001).
16. Z. Moser, W. Gasior, F. Sommer, G. Schwitzgebel, and B. Predel, *Metall. Trans. B* 17, 791. (1986).
17. D.K. Xu, B.J. Wang, C.Q. Li, T.T. Zu, and E.H. Han, *Mater. Des.* 69, 124. (2015).
18. D.K. Xu, C.Q. Li, B.J. Wang, and E.H. Han, *Mater. Des.* 88, 88. (2015).
19. N. Rahulan, S. Gopalan, and S. Kumaran, *Mater. Today-Proc.* 5, 17935. (2018).
20. J. Wang, L. Xu, R. Wu, J. Feng, J. Zhang, L. Hou, and M. Zhang, *Acta Metall. Sin-Engl.* 33, 490. (2020).
21. R. Mahmudi, M. Shalbafi, M. Karami, and A.R. Geranmayeh, *Mater. Des.* 75, 184. (2015).
22. Y. Ma, D. Cuiuri, N. Hoye, H. Li, and Z. Pan, *Mater. Sci. Eng. A.* 631, 230. (2015).
23. A.A. Nayeb-Hashemi, J.B. Clark, and A.D. Pelton, *Bull. Alloy Phase Diagrams* 5, 365. (1984).
24. R. Wu, Y. Yan, G. Wang, L.E. Murr, W. Han, Z. Zhang, and M. Zhang, *Int. Mater. Rev.* 60, 65. (2015).
25. Q.X. Shi, L.P. Bian, W. Liang, Z.Q. Chen, F.Q. Yang, and Y.D. Wang, *J. Alloys Compd.* 631, 129. (2015).
26. Z. Drozd, Z. Trojanová, and S. Kúdela, *J. Alloys Compd.* 378, 192. (2004).
27. S. Jin, H. Liu, R. Wu, F. Zhong, and L. Hou, Zhang. *J. Mater. Sci. Eng. A* 788, 139611. (2020).
28. Y. Wang, S. Zhang, R. Wu, N. Turakhodjaev, L. Hou, J. Zhang, and S. Betsofen, *J. Mater. Sci. Technol.* 61, 197. (2021).
29. R. Islam, and M. Haghshenas, *J. Magnes. Alloy.* 7, 203. (2019).
30. X.W. Wei, X.T. Zu, and W.L. Zhou, *Mater. Sci. Tech.* 22, 730. (2006).
31. Z. Zhao, X. Xing, Y. Luo, Y. Wang, and W. Liang, *J. Iron Steel Res. Int.* 24, 426. (2017).
32. S. Tang, T.Z. Xin, W.Q. Xu, D. Miskovic, G. Sha, Z. Quadir, S. Ringer, K. Nomoto, N. Birbilis, and M. Ferry, *Nat. Commun.* 10, 1003. (2019).
33. T. Liu, S.D. Wu, S.X. Li, and P.J. Li, *Mater. Sci. Eng. A* 460, 499. (2007).
34. F. Cao, F. Xia, H. Hou, H. Ding, and Z. Li, *Mater. Sci. Eng. A* 637, 89. (2015).
35. B. Jiang, Y. Zeng, M.X. Zhang, J.C. Liao, and F.S. Pan, *J. Mater. Res.* 28, 2694. (2013).
36. Y.D. Huang, W.M. Gan, K.U. Kainer, and N. Hort, *J. Magnes. Alloy.* 2, 1. (2014).